文章编号:0253-2778(2020)04-0418-10

A modified coherent diffraction algorithm based on the total variation algorithm for insufficient data

JIANG Qi, LIU Jianhong, GUAN Yong, BAI Haobo, LIU Gang, TIAN Yangchao
(*National Synchrotron Radiation Laboratory, University of Science and Technology of China, Hefei* 230029, *China*)

Abstract: X-ray coherent diffraction imaging (CDI) is a lensless imaging technology. Its basic principle is to illuminate an isolated sample with a highly coherent X-ray beam, then collect the information of the coherent diffraction pattern in the far field, and last restore the real structure information of the sample from the diffraction pattern by using the the CDI algorithm. Due to the limitation of experimental technology experimental data are usually defective, thus tolerance to noise and missing data is an important indicator for the CDI algorithm. Here a modified coherent diffraction algorithm by adding the total variation (TV) constraint into the CDI reconstruction algorithm was developed to improve the tolerance to noise and missing data. Then the performance of the modified coherent diffraction algorithm based on the total variation algorithm was verified using simulation data and experimental data. The results show the modified algorithm can accelerate convergence and improve the tolerance to noise and missing data.

Key words: coherent diffraction imaging; total variation; missing data; noise; constraint
CLC number: O436.1;TP391.41 **Document code**: A doi:10.3969/j.issn.0253-2778.2020.04.005

Citation: JIANG Qi, LIU Jianhong, GUAN Yong, et al. A modified coherent diffraction algorithm based on the total variation algorithm for insufficient data[J]. Journal of University of Science and Technology of China, 2020,50(4):418-427.
江琦,刘建宏,关勇,等. 一种针对不完善数据的基于全变分约束的相干衍射算法[J]. 中国科学技术大学学报,2020,50(4):418-427.

一种针对不完善数据的基于全变分约束的相干衍射算法

江 琦,刘建宏,关 勇,白浩波,刘 刚,田扬超

(中国科学技术大学国家同步辐射实验室,安徽合肥 230029)

摘要:X射线相干衍射成像(coherent diffraction imaging,CDI)技术是一种无透镜成像技术.其基本原理是使用高度相干的X射线光束照射孤立样品,在远场收集相干衍射图样的信息,使用CDI重构算法从衍射图样中还原出样品的真实结构信息.但是由于实验技术的限制,通常实验数据都是不完善的,所以相干衍射算法对于噪声和数据缺失的容忍能力是非常重要的.通过将全变分约束引入到CDI重构算法中得到了一种改进后的算法,以提升算法对噪声和数据缺失的容忍能力.并使用模拟数据与真实实验数据来进行验证,结果表明改进后算法可以加快算法的收敛速度以及提高对噪声和数据缺失的容忍能力.

关键词:相干衍射成像;全变分;数据丢失;噪声;约束

Received: 2019-05-21; **Revised**: 2019-06-22
Foundation item: Supported by National Key Research and Development Project of China (2017YFA0402904, 2016YFA0400902), National Natural Science Foundation of China (11475175, 11405175, 11275204,11775224).
Biography: JIANG Qi, male, born in 1994, master. Research field: Coherent diffraction imaging. E-mail: jqi1994@mail.ustc.edu.cn
Corresponding author: TIAN Yangchao, PhD/Prof. E-mail: ychtian@ustc.edu.cn

0 Introduction

In 1999, Miao et al.[1] experimentally realized coherent diffraction imaging (CDI) of aperiodic structures for the first time. Because of the construction of third-generation synchrotron radiation sources, coherent diffraction imaging, a lenless method[2], has been widely used in biology and material science[3-4]. A variety of reconstruction algorithms have been developed based on the Gerchberg-Saxton algorithm, such as error-reduction (ER) algorithm, hybrid input-output (HIO) algorithm, guide HIO (GHIO) algorithm, oversampling smoothness (OSS) algorithm. The basic principle of these algorithms is that different constraints are used to guide the direction of iteration for achieving the purpose of the improved algorithm. The TV-based CDI reconstruction algorithm follows the same improved route. From the current theory of CDI, data analysis for coherent X-ray imaging(CXI) is still a far from fully developed and enhanced algorithms based on new constraints. X-ray CDI involves irradiating a nonperiodic sample with X-rays, collecting the coherent diffraction image at the far field, and using a phase retrieval algorithm to obtain a high-resolution image of the sample[5]. These steps show that there are two main factors that affect the reconstruction of a coherent diffraction image: the quality of the acquired diffraction pattern and the ability of the phase retrieval algorithm. Therefore, for better CDI reconstruction results, we need to focus on two aspects: optimize experimental methods and improve the experimental system to obtain higher-quality diffraction patterns, and optimize phase retrieval and reconstruction algorithms to obtain the reconstructed structure.

In real circumstances, noise and missing data in the central area of the image often negatively affect the reconstruction of the image of the sample[6]. The noise level in actual experiments can easily reach 25% or higher, which is challenging for many reconstruction algorithms. The following theory about the missing data problem has been proposed:

$$\eta_i = \frac{D_i - 1}{2\sigma_i}, i = x, y, z \tag{1}$$

where D_i is the number of missing pixels in the i direction, i represents different diffraction directions, σ_i is the oversampling rate, and η_i is the number of missing waves. For example, if the oversampling rate of a diffraction pattern in the x direction σ_x is 3, then if the lost pixels in the x direction D_i is 7, the number of missing wave $\eta_x = 1$. When $\eta_i > 1$, some structural information about the sample has been permanently lost, which introduces artifacts into the reconstructed images. The missing structural information cannot be recovered by iterative algorithms. Therefore, an optimized phase retrieval and reconstruction algorithm that is more accurate with respect to noise and missing data in central area plays an important role in improving the resolution of reconstructed images[7]. This paper presents a reconstruction algorithm based on total variation (TV) constraints. According to the reconstruction results obtained with simulated data and experimental data, the reconstruction algorithm accelerates the convergence speed and improves the tolerance to noise and missing data in the central area.

1 TV-based CDI reconstruction algorithm

1.1 CDI reconstruction algorithm

Many CDI reconstruction algorithms are based on iteration between real space and reciprocal space. Different reconstruction algorithms have different constraints or filters in real space and reciprocal space. Taking the commonly used hybrid input-output(HIO) algorithm[8] and the oversampling smoothness (OSS) algorithm[9] as examples, the real-space constraints of the HIO algorithm are a finite-size constraint and a positive-density constraint, that is, a support constraint, and the reciprocal-space constraint is the amplitude constraint of the experimental data. A smoothing filter based on the HIO algorithm was added to the OSS algorithm. The process for the HIO algorithm is shown in Fig. 1.

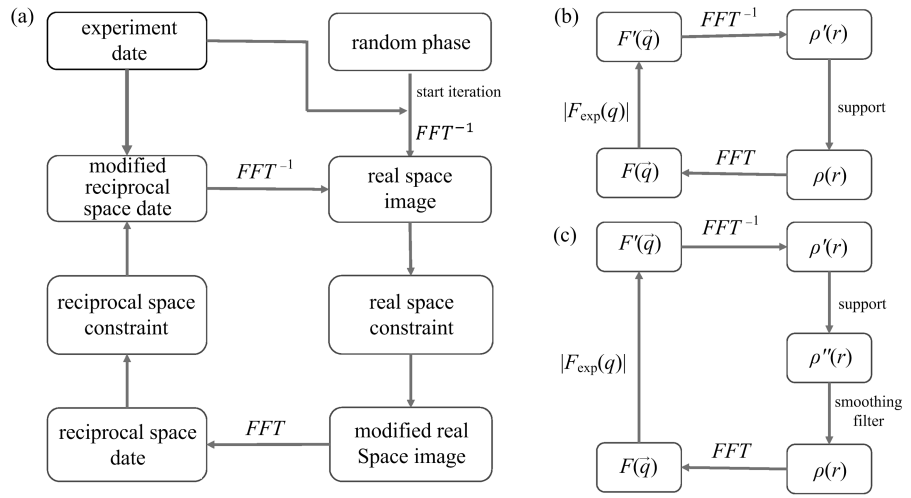

Fig. 1 (a) CDI iterative algorithm flowchart and (b) HIO algorithm flowchart that corresponds to (a). $|F_{exp}(q)|$ is the experimentally measured amplitude, which is the reciprocal space constraint; the support constraint is the real-space constraint, and $\rho(r)$ is the reconstruction result of each iteration. (c) OSS algorithm flowchart in which a smoothing filter based on (b) was added

1.2 TV principle

The usual theory of image reconstruction involves a transformation:

$$\boldsymbol{WX}=\boldsymbol{Y} \tag{2}$$

where $\boldsymbol{W}$ is the system matrix $[W_{i,j}]_{N\times M}$ composed of N row vectors $\boldsymbol{W}_i$, $\boldsymbol{X}$ is the unknown image, and $\boldsymbol{Y}$ is the experimental data, i. e., the diffraction pattern. In theory, the image $\boldsymbol{X}$ that needs to be reconstructed can be obtained directly with Eq. (2). However, the measured experimental data are usually insufficient[10], so a new method to solve this issue must be developed.

To solve the problem of Eq. (2), TV minimization was considered an effective method for obtaining high-quality reconstructed images from insufficient data. The idea of minimizing TV is to find an $\boldsymbol{X}$ that satisfies the following:

$$\min \| \boldsymbol{X}_{\mathrm{TV}} \| = \min \sum_{s,t} | \vec{\nabla} X_{s,t} |$$
$$\text{s. t. } \boldsymbol{WX}=\boldsymbol{Y} \tag{3}$$

If the pixel values are labeled $X_{s,t}$ then the image gradient magnitude, also known as the gradient image[11], is

$$| \vec{\nabla} X_{s,t} |=\sqrt{(X_{s,t}-X_{s-1,t})^2+(X_{s,t}-X_{s,t-1})^2} \tag{4}$$

The TV of the image is the l_1-norm of the gradient image, as shown in Eq. (5):

$$\| X_{s,t} \|_{\mathrm{TV}}=\sum_{s,t} | \vec{\nabla} X_{s,t} |= \sum_{s,t} \sqrt{(X_{s,t}-X_{s-1,t})^2+(X_{s,t}-X_{s,t-1})^2} \tag{5}$$

Minimization of TV is a useful way to reduce noise while preserving the edge in the image processing field. The mainstream method used to minimize TV is the gradient descent method, where the gradient of the image is defined as

$$G_{s,t}=\frac{\partial \| X \|_{\mathrm{TV}}}{\partial X_{s,t}} \approx \frac{(X_{s,t}-X_{s-1,t})+(X_{s,t}-X_{s,t-1})}{\sqrt{\varepsilon+(X_{s,t}-X_{s-1,t})^2+(X_{s,t}-X_{s,t-1})^2}} - \frac{(X_{s+1,t}-X_{s,t})}{\sqrt{\varepsilon+(X_{s+1,t}-X_{s,t})^2+(X_{s+1,t}-X_{s+1,t-1})^2}} - \frac{(X_{s+1,t}-X_{s,t})}{\sqrt{\varepsilon+(X_{s,t+1}-X_{s,t})^2+(X_{s,t+1}-X_{s-1,t+1})^2}} \tag{6}$$

where ε is a small positive number ($\varepsilon=1\times10^{-8}$) added to the denominator to prevent the special case where the denominator is zero.

According to a TV-based algorithm for recovering an image from sparse samples of its Fourier transform[11]. The premise that this optimization method is effective is that the gradient image of the sample is sparse. If the number of pixels in a picture with zero or near zero is twice the number of non-zero pixels, then this picture is sparse.

1.3 TV-CDI reconstruction algorithm

As shown in Fig. 2, TV constraint was added

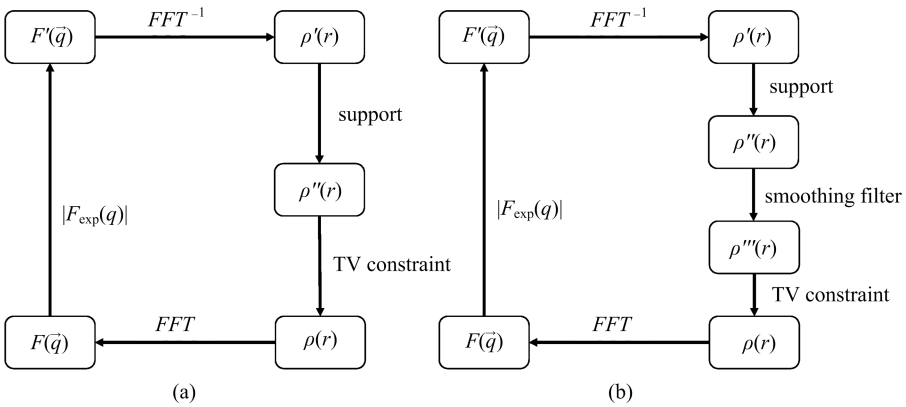

Fig. 2　(a) TV-HIO algorithm flowchart and (b) TV-OSS algorithm flowchart where the TV constraint was added to

to the CDI reconstruction algorithm on the basis of the TV-based gradient descent reconstruction algorithm (POCS-TVM)[11]. TV constraint plays a role in guiding the direction of iteration.

The TV gradient descent constraint is defined as

$$\left.\begin{aligned} d_A &= |\rho'_i(r)-\rho''_i(r)|, \vec{G}_{s,t}(r)=\frac{\partial \|\vec{X}\|_{TV}}{\partial X_{s,t}}, \\ G(r) &= \frac{\vec{G}(r)}{|\vec{G}(r)|}, \rho'''_i(r)=\rho''_i(r)-\alpha d_A G(r) \end{aligned}\right\} \tag{7}$$

where d_A is the difference factor between the reconstructed image of the last iteration and the image after the support constraint, α is a relaxation factor, and $\rho'_i(r)$ and $\rho''_i(r)$ are real-space sample images reconstructed at different stages of the algorithm. Eq. (7) shows that the TV constraint can be added to any CDI iterative reconstruction algorithm. The original HIO and OSS algorithms had a TV constraint added to their flowcharts to yield TV-HIO and TV-OSS.

2　Simulation results

To verify the effectiveness of the algorithm, we performed a series of simulation experiments using different noise intensities and different amounts of missing data in the central area. We used the HIO, TV-HIO, OSS, and TV-OSS algorithms to reconstruct the image and compared the results of the original algorithms with the reconstruction results of the algorithms with the TV constraint.

As shown in Fig. 3, the original image used in the simulation experiment was a "Lena" image (256×256 pixels) and the oversampling rate was set to 3.16 independent calculations for each case were performed. Considering the quality of reconstruction and calculation time, the TV constraint was used every five iterations and the gradient descent was calculated 10 times for each TV constraint. The relaxation factor α in the TV constraint was 0.2 and the relaxation factor β in the support constraint was 0.8. We performed 10 000 iterations and finished the reconstruction with 100 iterations of the error-reduction (ER) algorithm to let the algorithm converge to the closest local minimum[12-13].

As shown in Figs. 4 and 5, we added five levels of Poisson noise, 5%, 10%, 15%, 20%, and 25% separately, into the simulated diffraction patterns. The average number of photons per pixel in the central area of 100×100 pixels region of the diffraction pattern with the above five different noise was calculated, it is 4.2×10^4, 1.06×10^4, 4.27×10^3, 2.37×10^3, 1.5×10^3 photons per pixel respectively. The four levels of missing data at the center, 7×7, 10×10, 13×13, and 19×19 pixels, were set separately.

The noise intensity was calculated as follows:

$$R_{noise}=\frac{\sum\limits_{\vec{k}-\vec{k}_{low}} \left| |F_{noise\text{-}free}(\vec{k})|-|F_{noise}(\vec{k})| \right|}{\sum\limits_{\vec{k}-\vec{k}_{low}} |F_{noise\text{-}free}(\vec{k})|} \tag{8}$$

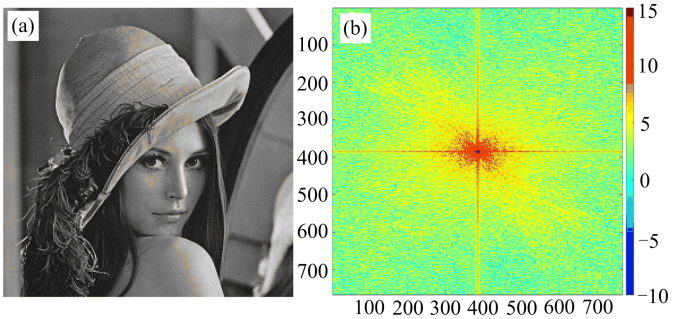

Fig. 3 （a）“Lena” image，256×256 pixels，and（b）simulated diffraction pattern，no noise

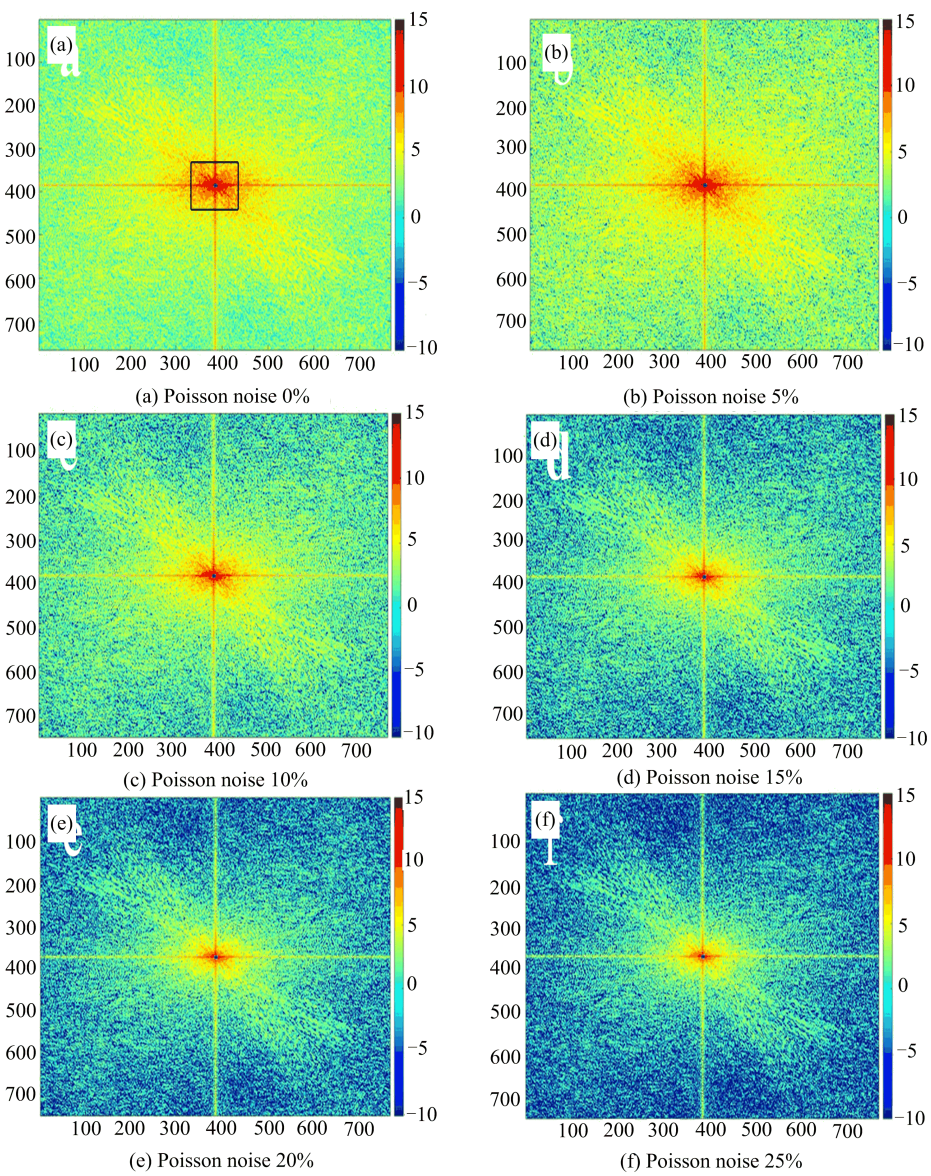

All sets have a 7×7 pixels data loss at the center. The black square area in (a) is the low frequency area that does not participate in the noise intensity calculation.

Fig. 4 Simulated patterns of Poisson noise in noise-free，5%，10%，15%，20%，and 25% intensity，respectively

where $|F_{\text{noise-free}}(\vec{k})|$ represents the noise-free Fourier magnitudes and $|F_{\text{noise}}(\vec{k})|$ represents the Fourier magnitudes with Poisson noise. Because more than 90% intensity of the pattern is located

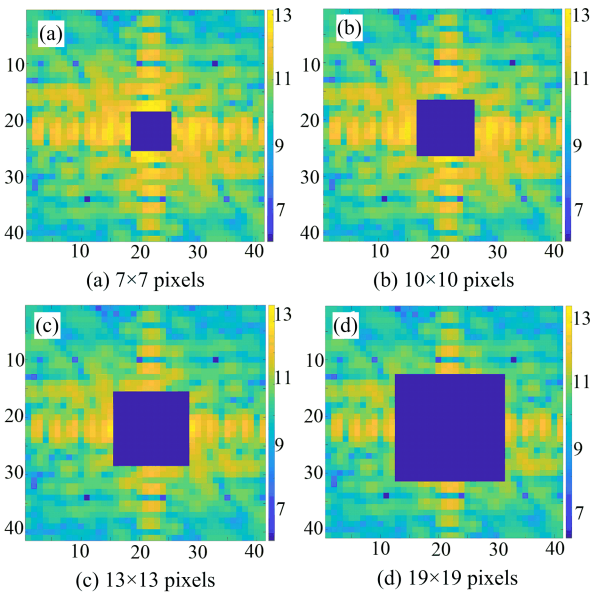

Fig. 5　Center of the enlarged diffraction pattern with data losses of 7×7, 10×10, 13×13, and 19×19 pixels, respectively

in the central low-frequency region and the Poisson noise affects mainly the high-frequency region, part of the central area data was not involved in the calculation. As an example, the pattern size of the simulation experiment was 768×768 pixels while the data in the central area of 100×100 pixels was not included in the calculation.

We used the real-space error coefficient as a criterion for judging the quality of reconstruction. It is defined as

$$R_{\text{error}} = \sum |X_{\text{rec}} - X_{\text{orig}}| / \sum X_{\text{orig}} \qquad (9)$$

where X_{rec} is the reconstructed image and X_{orig} is the original image. The real-space error coefficient can be used to see visually the degree of difference between the reconstructed image and the original image.

The results of our simulation experiments are presented in Tab. 1. The data show that under the same conditions, the real-space error coefficients of the reconstructed image after TV constraint are significantly reduced, which improves the accuracy of convergence and the tolerance to noise intensity and data loss in the central area.

The computational time required for the various algorithms to perform 10 000 iterations is presented in Tab. 2. The data show that adding the TV constraint increased the computational time by about 150 s for both HIO and OSS algorithms, increase 23% computational time for HIO while 11% for OSS. and there were no obvious correlations with other factors.

Tab. 1　Real-space error coefficients of the four algorithms under different simulation conditions

algorithm	pixels	missing data				
		5%	10%	15%	20%	25%
HIO	7×7	10.97%	12.75%	13.83%	14.73%	15.62%
	10×10	10.70%	12.80%	14.19%	15.39%	15.53%
	13×13	11.32%	13.02%	15.30%	16.56%	19.96%
	19×19	12.07%	19.33%	19.15%	20.69%	28.41%
TV-HIO	7×7	7.2%	10.81%	12.78%	13.85%	14.32%
	10×10	7.31%	11.05%	12.85%	13.80%	14.43%
	13×13	8.14%	11.56%	15.45%	14.86%	16.92%
	19×19	9.31%	13.33%	16.38%	20.64%	21.21%
OSS	7×7	7.82%	9.42%	10.97%	11.85%	12.72%
	10×10	7.84%	9.49%	11.0%	11.61%	11.92%
	13×13	7.85%	9.86%	10.71%	12.52%	12.68%
	19×19	11.13%	11.42%	11.23%	13.09%	15.66%
TV-OSS	7×7	1.67%	3.21%	5.66%	7.46%	9.08%
	10×10	1.62%	3.27%	5.88%	7.60%	9.27%
	13×13	2.17%	3.74%	5.94%	8.94%	9.62%
	19×19	3.25%	5.46%	6.95%	10.42%	11.85%

Tab. 2 Computational time for 10 000 iterations of the four algorithms under different conditions (unit:s)

algorithm	pixels	missing date				
		5%	10%	15%	20%	25%
HIO	7×7	646.80	642.68	646.56	666.21	670.96
	10×10	647.28	645.27	648.61	651.78	652.35
	13×13	649.73	647.41	649.58	650.79	650.37
	19×19	648.73	649.79	650.35	651.01	649.83
TV-HIO	7×7	787.50	791.97	792.77	794.11	795.97
	10×10	787.47	792.09	797.11	797.99	796.96
	13×13	787.58	790.78	792.92	793.17	798.01
	19×19	789.00	790.70	796.59	798.96	792.92
OSS	7×7	1295.75	1300.86	1301.94	1292.11	1293.57
	10×10	1296.57	1298.27	1292.46	1294.68	1299.11
	13×13	1292.69	1298.92	1321.99	1295.48	1302.52
	19×19	1298.15	1295.28	1293.92	1302.34	1299.78
TV-OSS	7×7	1446.38	1453.81	1445.78	1440.77	1448.53
	10×10	1459.44	1452.48	1457.28	1440.66	1445.68
	13×13	1448.84	1450.80	1456.86	1445.68	1439.76
	19×19	1453.78	1452.56	1434.28	1448.60	1437.60

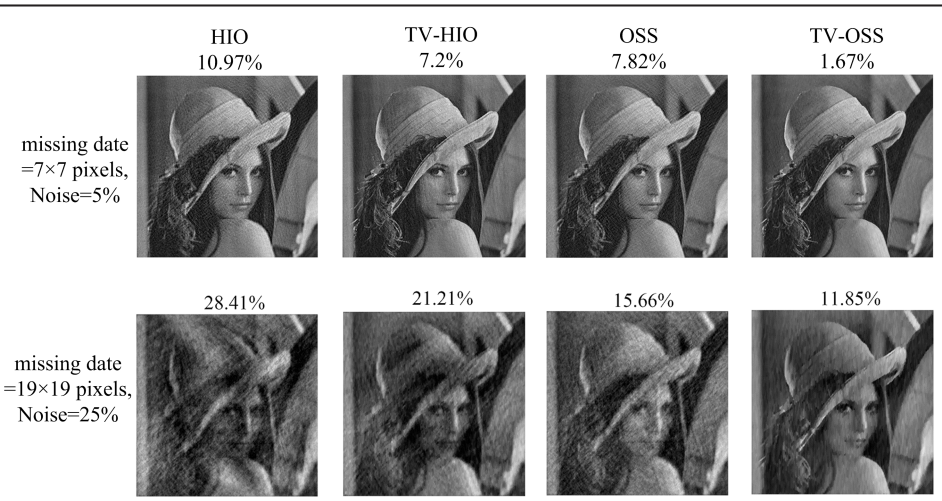

Fig. 6 Reconstruction results and reconstruction error coefficients of the four algorithms obtained under the best and worst simulation conditions

To see the contrast more intuitively, we selected the reconstructed images obtained under the best and the worst simulation conditions, shown in Fig. 6.

Under the best simulation conditions, the four algorithms basically reconstructed a clear image, but the real-space error coefficient and visual perception show that adding the TV constraint improved the reconstruction quality and accuracy. Under the worst simulation conditions, the real-space error coefficient of the HIO algorithm was as high as 30%, which basically announced the failure of the reconstruction. After adding the TV constraint, we see a clear outline of "Lena",

confirming the improvement of the reconstruction quality. The reconstruction result of the TV-OSS algorithm was very good, even under the worst simulation conditions. The real-space error coefficient almost reached the reconstruction precision of the HIO algorithm under the best simulation conditions.

3 Experiment data reconstruction

To further demonstrate the advancement of the algorithm, we used the diffraction pattern from a CDI experiment on magnetotactic bacteria, shown in Fig. 7[14]. This diffraction pattern is obtained after a series of pre-processing steps and can be directly reconstructed. Compared with Fig. 4, we can find that the noise of this diffraction pattern is relatively high.

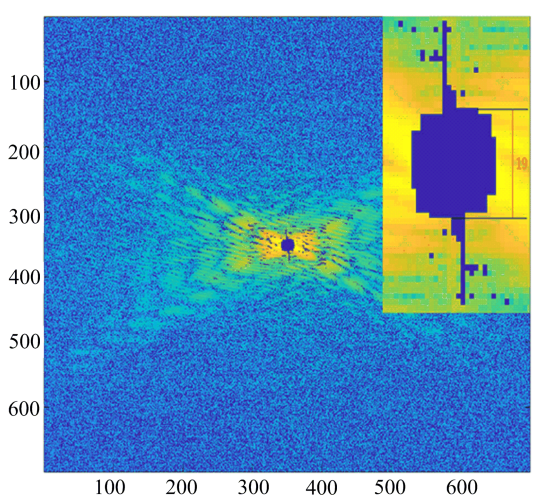

Fig. 7　The 700 × 700 pixels diffraction pattern of the magnetotactic bacteria. The inset is the center of the enlarged diffraction pattern, where the data loss is 19 × 19 pixels

According to the theory on oversampling, we can estimate the oversampling rate in the horizontal and vertical directions. After calculation, the oversampling rate was 11.7 in the horizontal and 3.4 in the vertical. Therefore, we started with loose support of 200 × 60 pixels, then obtained tighter support from the dozens of reconstruction images with loose support by setting the intensity threshold. By repeating this process, tighter support was obtained, as shown in Fig. 8.

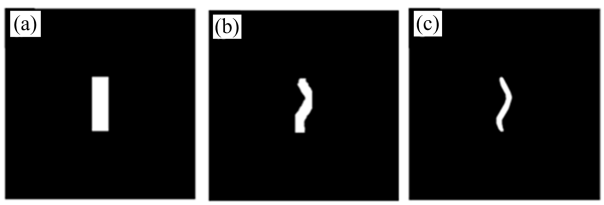

Fig. 8　Tight support and loose support used in the reconstruction process

The four algorithms were used to reconstruct the diffraction pattern of the magnetotactic bacteria shown in Fig. 7. The results, which are roughly similar, are shown in Fig. 9. Compared with the results of Ref. [14], the reconstruction results show that the reconstructed contour is reliable. In a real experiment, the real-space error cannot be calculated and additional parameters are required to measure the quality of reconstruction. The most commonly used convergence consistency of the reconstruction results and the phase retrieval transfer function are methods that meet our needs.

Each of the four algorithms performed 200 independent reconstructions and the convergence of the reconstruction results was analyzed. The difference between the 200 results of each reconstruction algorithm is calculated as follows:

$$\begin{cases} D_{s,t} = \dfrac{\sum\limits_{x,y} |\rho_s(x,y) - \rho_t(x,y)|}{\sum\limits_{x,y} |\rho_s(x,y) + \rho_t(x,y)|}, \\ (s,t = 1,2,3,\cdots,200) \cap (s \neq t) \end{cases} \tag{10}$$

The smaller the difference, the better the convergence of the reconstruction result. After fitting the difference between the 200 results, the reconstruction convergence of the four algorithms becomes intuitive. The fitting curve is shown in Fig. 10, where the abscissa is the difference value and the ordinate is the probability distribution value as a function of the difference value. The smaller the difference in the peak of the fitting curve and the smaller the half-height width, the better the convergence of the reconstruction result. After adding the TV constraint, the convergence improved, which agrees with the

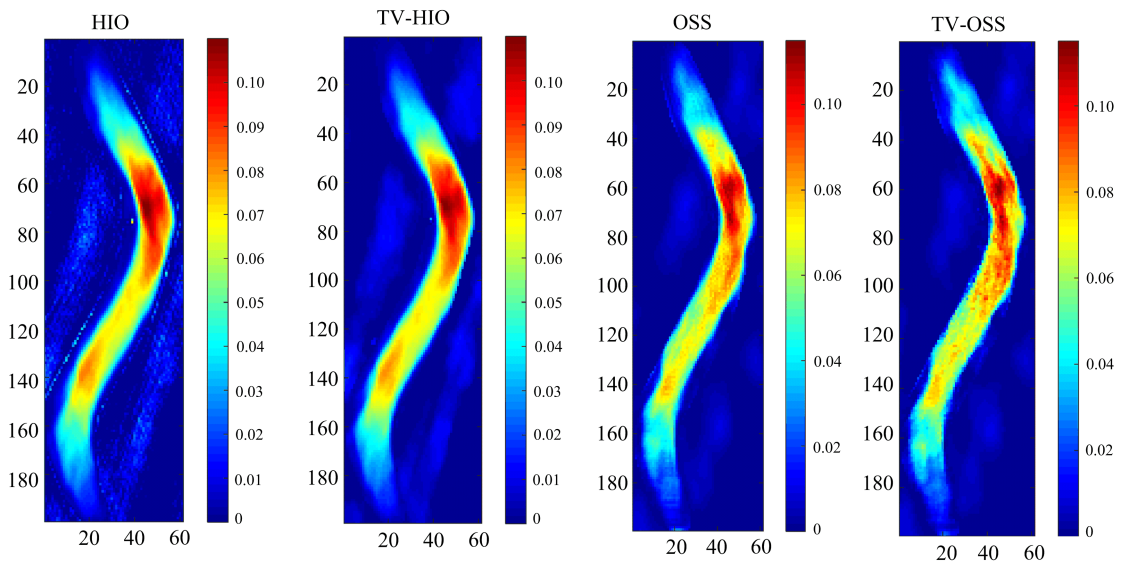

Fig. 9 Average of 200 reconstruction results of the four algorithms

expected results of the simulation experiment.

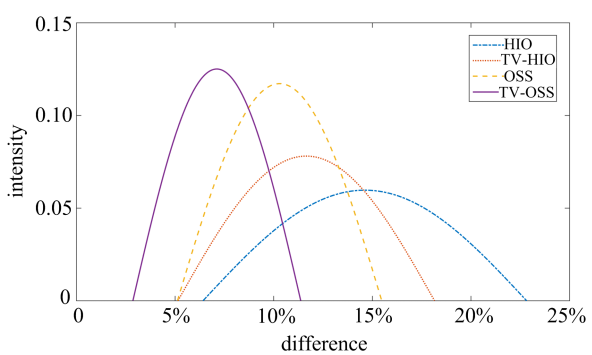

Fig. 10 Fitting curve of convergence of the four algorithms

In addition to verifying the accuracy of the reconstruction by the algorithms, we calculated the phase retrieval transfer function (PRTF) curve of the reconstruction results of the four algorithms as follows[16]:

$$\mathrm{PRTF}(q)=\frac{|F_{\mathrm{cal}}|}{|F_{\mathrm{exp}}|} \tag{11}$$

where $|F_{\mathrm{cal}}|^2$ is the diffraction pattern obtained by reversing the reconstruction result and $|F_{\mathrm{exp}}|^2$ is the experimentally measured diffraction pattern, which is equal to the square of the amplitude. The PRTFs of the reconstruction results of the four algorithms are shown in Fig. 11, where the red horizontal line is the reference value of $1/e$[16] and 0.5. The figure shows that the reconstruction results of the OSS and TV-OSS algorithms were significantly better than those of the HIO and TV-HIO algorithms and that results of the TV-HIO algorithm were better than those of the HIO algorithm. The reference value shows that the reconstruction results of the OSS and TV-OSS algorithms are reliable. From Fig. 11, we can draw the conclusion that the reconstruction was more accurate after adding TV constraints.

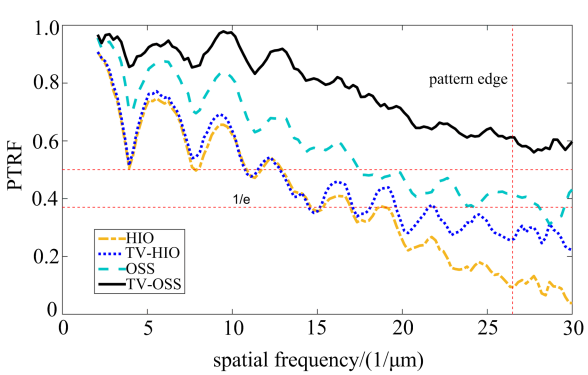

Fig. 11 PRTF curves of the reconstruction results of the four algorithms

4 Conclusion

We presented our proposal of a new constraint called total variation (TV) minimization that can be added to any coherent diffraction iterative reconstruction algorithm. We added the TV constraint to the popular HIO and OSS algorithms to yield the TV-HIO and TV-OSS algorithms. According to the reconstruction results using simulation data and experimental data, the

addition of the TV constraint improved the tolerance to noise and missing data, and improved the accuracy and consistency of the reconstructed image.

In addition, because the TV algorithm is an iterative algorithm, it is easy to add it to an iterative reconstruction algorithm. TV minimization can be added to the PIE algorithm[17] and other coherent diffraction 3D reconstruction algorithms[3] that have wide range for development and application.

The TV-based CDI reconstruction algorithm had been developed on the basis of previous algorithms to improve the performance of the algorithm and provide more algorithm choices for experimenters. At present, this algorithm is only used in simulation data and biological cell experimental data. In the future, it will need to be continuously improved in the data processing process of different types of experimental samples.

Acknowledgments

We would like to thank Professor Jiang Huaidong from Shanghai University of Science and Technology for valuable suggestions and providing the experimental data of magnetotactic bacteria.

References

[1] MIAO J W, CHARALAMBOUS P, KIRZ J, et al. Extending the methodology of X-ray crystallography to allow imaging of micrometer-sized non-crystalline specimens[J]. Nature, 1999, 400: 342-344.

[2] ROY M, SEO D, OH S, et al. A review of recent progress in lens-free imaging and sensing [J]. Biosensors and Bioelectronics, 2017, 88: 130-143.

[3] JIANG H D, SONG C Y, CHEN C C, et al. Quantitative 3D imaging of whole, unstained cells by using X-ray diffraction microscopy[J]. Proc Natl Acad Sci U S A, 2010, 107(25): 11234-11239.

[4] MIAO J W, NISHINO Y, KOHMURA Y, et al. Quantitative image reconstruction of GaN quantum dots from oversampled diffraction intensities alone[J]. Phys Rev Lett, 2005, 95(8): 085503.

[5] CHAPMAN H N, NUGENT K A. Coherent lensless X-ray imaging[J]. Nat Photonics, 2010, 4(12): 833-839.

[6] HUANG X J, NELSON J, STEINBRENER J, et al. Incorrect support and missing center tolerances of phasing algorithms[J]. Opt Express, 2010, 18(25): 26441-26449.

[7] SHAPIRO D, THIBAULT P, BEETZ T, et al. Biological imaging by soft X-ray diffraction microscopy [J]. Proc Natl Acad Sci U S A, 2005, 102(43): 15343-15346.

[8] FIENUP J R. Phase retrieval algorithms: A comparison [J]. Appl Optics, 1982, 21 (15): 2758-2769.

[9] RODRIGUEZ J A, XU R, CHEN C C, et al. Oversampling smoothness: An effective algorithm for phase retrieval of noisy diffraction intensities [J]. J Appl Crystallogr, 2013, 46: 312-318.

[10] XU R, SALHA S, RAINES K S, et al. Coherent diffraction microscopy at SPring-8: Instrumentation, data acquisition and data analysis [J]. J Synchrot Radiat, 2011, 18: 293-298.

[11] SIDKY E M, KAO C M, PAN X C. Accurate image reconstruction from few views and limitedangle data in divergentbeam CT[J]. J X-Ray Sci Technol, 2006, 14 (2): 119-139.

[12] VAN DER SCHOT G, SVENDA M, MAIA F, et al. Imaging single cells in a beam of live cyanobacteria with an X-ray laser [J]. Nat Commun, 2015, 6 (9): 5704.

[13] GERCHBERG R W, SAXTON W O. Practical algorithm for determination of phase from image and diffraction plane pictures [J]. Optik: International Journal for Light and Electron Optics, 1972, 35(2): 237-250.

[14] FAN J D, SUN Z, ZHANG J, et al. Quantitative imaging of single unstained magnetotactic bacteria by coherent X-ray diffraction microscopy[J]. Anal Chem, 2015, 87(12): 5849-5853.

[15] MIAO J W, HODGSON K O, ISHIKAWA T, et al. Imaging whole *Escherichia coli* bacteria by using single-particle X-ray diffraction[J]. Proc Natl Acad Sci U S A, 2003, 100(1): 110-112.

[16] CHAPMAN H N, BARTY A, MARCHESINI S, et al. High-resolution ab initio three-dimensional X-ray diffraction microscopy [J] . J Opt Soc Am A: Opt Image Sci Vis, 2006, 23(5): 1179-1200.

[17] PFEIFFER F. X-ray ptychography[J]. Nat Photonics, 2017, 12(1): 9-17.